Blast wave propagation in survival shelters: Experimental analysis and numerical modelling

Shock Waves manuscript No.
(will be inserted by the editor)

Blast wave propagation in survival shelters: Experimental analysis and numerical modelling

A. Caçoilo[1,2] · **F. Teixeira-Dias**[2] · **R. Mourão**[1,2] · **B. Belkassem**[1] · **J. Vantomme**[1] · **D. Lecompte**[1]

Received: date / Accepted: date

Abstract The propagation of blast and shock waves in confined environments is a complex phenomenon; yet, being able to derive valid predictions of such phenomena is highly relevant, for example, when it comes to the assessment of protection of personnel in military environments. This study looks at the propagation of blast waves inside a compound survival shelter. Experimental analyses are performed on a small-scale model of the actual configuration of the shelter subjected to the detonation of an explosive charge at different locations close to its entrance. Pressure-time signals are recorded on a number of locations in the model. A numerical model is also developed to complement the experimental program, based on the explicit finite element (FE) code LS-DYNA. The recorded experimental data (e.g., pressure and impulse) are compared with the numerical predictions to validate the FE model. The authors discuss two different modelling approaches (the Lagrangian and the MM-ALE formulations) and analyse the influence of using a different number of ambient layers, the advection method, the time-step size, and level of discretisation. The proposed numerical model predicts and captures the relevant stages of the propagation of the shock wave very well, with error levels on the resulting specific impulse always lower than 19% when compared to the experimental observations.

Keywords Blast wave · Shock wave · Small-scale models · Confined explosions · Experimental analysis · Numerical modelling · LS-DYNA

1 Introduction

The safety of both personnel and equipment in unstable regions has for a long time been a major issue and concern. One way of protecting personnel and sensitive equipment is to use protective shelters with corner-entrance or flow-through configurations. It is important to know the response of such shielding structures to blast waves. Military compounds are vulnerable to different types of threats such as mortar strikes, Improvised Explosive Devices (IED), Vehicle-Borne Improvised Explosive Devices (VBIED), among others. The generic

F. Teixeira-Dias, E-mail: F.Teixeira-Dias@ed.ac.uk
[1] Civil and Materials Engineering Department, Royal Military Academy, Brussels, Belgium
[2] Institute for Infrastructure and Environment (IIE), School of Engineering, The University of Edinburgh, Edinburgh EH9 3JL, UK

type of protective shelter analysed in this work is used to rapidly build a defensive compound. It is based on the standard ISO 20 ft sea container and the Hesco-Bastion gabions. An example of such a system is shown in Figure 1. The entire structure is highly flexible in design, allowing separate modules to be attached to each other in a number of different configurations.

Fig. 1 Hesco-Bastion survival shelter configuration during construction [1].

Free-air propagation of shock waves is well known and understood; extensive technical and scientific resources can be found in the literature to support this, such as the reference works of Kinney and Graham [2] from the early 1960s and Baker et al. [3] from the 1980s. Analytical, empirical and numerical tools have been developed to predict the pressure flow generated by the free-air detonation of a high-explosive. However, only a limited number of publications can be found on the study of blast wave propagation in confined environments, which is the case of the protective structures described above. For such scenarios, classical analytical solutions are either not valid or limited due to the complex behaviour of the blast wave, caused by multiple reflections and spurious effects [4].

Confined explosions have, however, been studied in different settings such as urban environments [1,5–9], tunnels [10–12], and small-size closed compartments and rooms [4, 13–16], where the flow of blast waves is constrained by obstacles and non-straight narrow paths.

Reflections and channelling effects have also been investigated in urban scenarios. Fouchier *et al.* [9] studied the effects of typical urban configurations (open roads, T-junctions and other junction configurations, and the channelling effect) on the blast propagation. Results show that the most critical situation in case of the detonation of a high-explosive in an urban environment is the presence of narrow and straight roads with high buildings, since the

blast overpressure and consequent impulse can be significantly increased with the degree of confinement. Smith *et al.* [11] performed a detailed experimental campaign to measure the blast wave parameters in tunnel environments with complex configurations. The results of small-scale (1:45) smooth-walled tunnels of differing geometry were then compared with real-size models, where a good correlation in terms of peak overpressure was obtained. Rigas *et al.* [12] have also looked at shock wave propagation in branched tunnels. They found that the blast wave preserves supersonic speed along narrow tunnels. The work indicates that long narrow geometries and configurations contribute to increasing the blast wave front velocity and pressure.

To better understand the influence of the degree of confinement of a structure around an explosion on the interaction and propagation of reflected shock waves, Sauvan *et al.* [13] considered the influence of progressively adding walls to a partially confined compartment. One of the major findings was that in a semi-confined environment, the negative phase of the blast wave can lead to more significant damage than the positive phase. Geretto *et al.* [14] presented an experimental analysis of square steel plates subjected to blast loading under three different confinement levels (free-air burst, fully vented, and fully confined). They concluded that the structural response is affected and the level of damage increases with the level of confinement.

Performing full-size experimental tests on threat scenarios that involve explosion events is very costly, time consuming, and raises serious safety concerns. To overcome this, the use of small-scale models to represent full-size configurations has been considered by a number of authors. This approach has been used over the last three decades [1,5–13] and, more recently, an attempt to describe the changes in the pressure history due to the detonation of a high-explosive charge in a confined environment composed of a four-room single-story building was made by Julien *et al.* [4]. These authors conducted a series of small-scale experiments based on a multi-chamber model and proposed a good analytical estimation of the maximum overpressure in the entire model as a function of the chamber volumes.

A complementary approach to the experimental analysis of such complex environments is the use of Finite Element Analysis (FEA). This numerical technique can lead to high computational costs related to the very high level of discretisation often necessary to capture the complex wave interactions and reflections [17]. Several authors have used these techniques, validated with small-scale experimental analyses, to assess the blast wave propagation in confined configurations [1,4,6,7,10,12,18]. Lecompte *et al.* [1] dedicated their attention to the evaluation of a modular laboratory-scale building system of a survival shelter using two different configurations — corner-entrance and flow-through — and corresponding numerical analyses. In general, the results have shown that the use of the modular building system (e.g., commercially available building bricks) is an acceptable and reasonably quick tool to build small-scale models.

This paper presents an experimental approach to surpass the problems found in the experimental work of Lecompte *et al.* [1]. This small-scale model construction method here proposed prevents the detachment of the inter-brick connections, allowing for a complete assessment of the blast wave propagation over time. Moreover, when the detachment of the inter-brick connections appear, the assumption of rigid walls is no longer valid and the recorded pressure values should no longer be considered reliable, as occurred in the study of Lecompte *et al.* [1].

As stated above, blast wave propagation in tunnels, urban scenarios, and confined geometries has been studied by several authors. Nevertheless, the propagation of the blast wave in complex confined environments, where a multiplicity of effects can take place, is still a relevant research topic. Within the above framework, this paper presents a combina-

tion of small-scale experimental tests and numerical analyses to understand the propagation of blast waves in complex confined environments such as the Hesco-Bastion shelter shown in Figure 1.

2 Experimental setup

A convenient way to reproduce the effects of the detonation of a high-explosive at laboratory-scale preserving the blast wave characteristics of the original event is to make use of blast wave scaling laws. These laws are based on the fundamentals of geometrical similarity and assume that the physical quantities of pressure and velocity remain unchanged in the scaling. The most widely used approach to scale a blast event is the well-known Hopkinson-Cranz scaling law, based on cube-root scaling [19],

$$Z = \frac{R}{\sqrt[3]{W}} \tag{1}$$

This approach makes use of the concept of scaled distance, where R is the stand-off distance and W is the mass of high-explosive. This relation establishes that similar blast waves are produced at identical scaled distances when two different charges of the same explosive and with the same geometry are detonated in the same atmosphere.

The main goal of the experimental tests presented here is to collect valuable data that can be used to validate a numerical model of the Hesco-Bastion compound (HBC) configuration. A representative small-scale model of the HBC is tested, based on the approach described above. The experimental set-up and conditions are described in detail in the following paragraphs.

The test set-up, shown in Figure 2, was designed with a geometrical reduction factor $\lambda = 10$, i.e., all dimensions and stand-off distances are scaled down by a factor of 10 relative to the full-scale HBC configuration.

The model structure — the ground, the ISO container, and the shelter — was built from plywood and fixed/connected using countersunk screws. For ease of manipulation, the model walls are hollow, as can be seen in Figure 2(a). Since wall deformations were neglected, the experimental results include an overestimation of pressure and impulse due to the conservation of mass, momentum, and energy.

The high-explosive charge was positioned in contact with the model's ground, leading to a contact detonation and a hemispherical surface burst, representative of a charge located at the entrance of the compound. To avoid excessive damage to the model at the location of the detonation, a support system composed of a foam block and the detonator was built underneath the model, allowing the charge to be positioned where necessary above the ground. A detailed view and a schematic representation of this support system are shown in Figures 2(c) and (e), respectively. It should be noted, however, that with this method part of the blast wave generated by the detonation is propagated below the surface of the experimental set-up, since it is located underneath the model supporting structure (table). As such, not all the explosive mass contributes to the hemispherical burst. To quantify this, a blast pencil was used and positioned 30 cm from the charge to measure the incident pressure and to estimate the actual mass of high-explosive that generates the pressure pulse impinging on the HBC model. This sensor can be seen in Figures 2(b) and (d).

A spherical charge with a total mass of 4.2 g of C4 high-explosive was used in all experiments. This high-explosive is characterised by a detonation velocity of 8092 m/s, a combined pressure/impulse TNT equivalent factor of 1.28 and a density of 1.73 g/cm^3

[3,20]. The ignition of the high-explosive was achieved with a M75 electrical detonator, containing the equivalent of 1 g of TNT.

Figure 3 shows the overpressure history as recorded by the blast pencil. The blast pencil measurements coupled with the Kingery-Bulmash empirical equations [21] were used to quantify the energy fraction that is lost underneath the base plate. The blast pressure acting on the structure is thus estimated to be equivalent to 3.3 g of TNT. Based on the scaling laws described above and a geometrical factor $\lambda = 10$, this is equivalent to a charge of 3.3 kg of TNT in the full-scale HBC configuration. The TNT equivalency is based on the measured incident pressure (279 kPa) and stand-off distance (30 cm) and was calculated in accordance with the TM5-855-1 empirical formulae for surface burst conditions [22].

A total of 20 PCB 102B pressure transducers were embedded on the walls of the container model to allow for the characterisation of the blast wave and its evolution within the HBC, and to assess the pressure profiles on the faces of the ISO container model. The exact location of the pressure transducers used in this work is shown in Figure 4(a).

Two different charge locations were used in the experimental tests, as shown in Figure 4(b). These were located along a 45° angle of incidence relative to the entrance of the HBC, at 0.5 and 1 m (scaled distances) from the entrance. The equivalent full-scale distances are 5 and 10 m.

3 Numerical modelling

3.1 Model description

Two approaches are commonly used when simulating structures subjected to blast loads: (i) the Lagrangian method, which involves applying empirical pressures resulting from the air blast directly to the model discretised using a Lagrangian mesh; and (ii) the Multi-Material Arbitrary Lagrangian-Eulerian (MM-ALE) approach, which involves explicitly modelling the air and explosive and assigning appropriate equations of state to the materials. Since the Lagrangian approach avoids modelling the air between the explosive and the structure, a significant reduction in computational time can be achieved. A method widely known as the coupled method [23] that combines the advantages of the Lagrangian and MM-ALE approaches is used in this work.

The coupling method includes the modelling of the surrounding air. However, instead of modelling the high-explosive and its detonation, an empirical blast pressure is applied on a single layer of elements of the ALE formulation. This is referred to as the *ambient layer*, which makes up the exterior surface of the air domain facing the blast, and acts as a connection with the air domain (see Figure 5(a)). The main purpose of the ambient layer is to act as a receptor of the blast wave parameters based on the Kingery-Bulmash empirical equations [21]. These parameters are then converted into thermodynamic state data, which are subsequently applied as a source onto the adjoining ALE finite elements [24]. The blast wave then propagates into the model and interacts with the structure, and the reflections and wave superpositions are captured by the ALE air elements.

This method is implemented in LS-DYNA with the keyword `*LOAD_BLAST_ENHANCED` (LBE), where the location and mass of the high-explosive charge can be defined. An adequate element formulation (`ELFORM=11`) and ambient element type (`AET=5`) must be specified for the single element layer (ambient layer) [25]. The ALE mesh is created to model the air domain inside the shelter. Since the walls of the shelter and container are assumed to

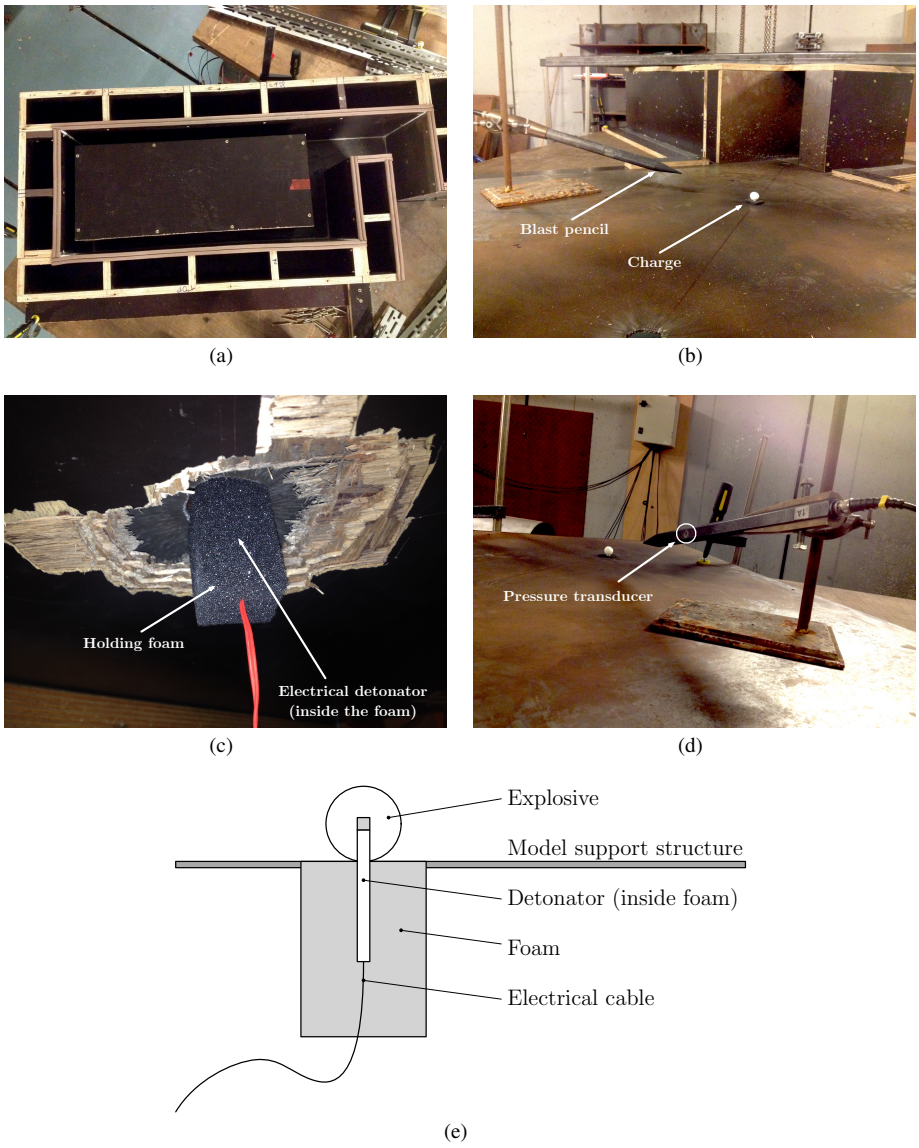

(a) (b) (c) (d) (e)

Fig. 2 Experimental small-scale set-up: (a) top view (with roof removed for clarity); (b) global view; (c) holding system (foam and electrical detonator); (d) blast pencil and location of the spherical high-explosive charge; (e) schematics of the high-explosive support system.

be rigid, both are modelled by restraining the boundary nodes of the air domain. This approach results in an efficient computational model, where a significant part of the air domain between the detonation and the structure is not explicitly considered.

A number of tracer points — the numerical equivalent to pressure gauges — are implemented at the same locations as in the experimental set-up in order to allow for the validation of the numerical model.

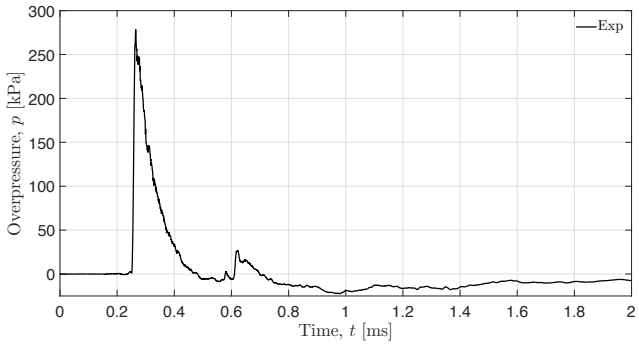

Fig. 3 Overpressure history measured by the blast pencil (see location of blast pencil in Figure 2).

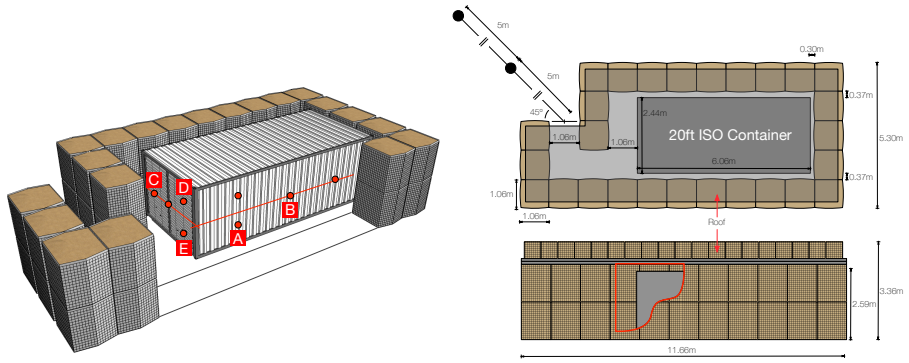

(a) (b)

Fig. 4 Full-scale model of the survival shelter: (a) 3-dimensional (3D) view of the HBC configuration and location of the pressure sensors (roof not shown for clarity), and (b) 2-dimensional (2D) top and side views of the HBC with the location of the high-explosive charges. All linear dimensions of the small-scale model used in experiments (see Figure 2) are scaled down by a factor of 10.

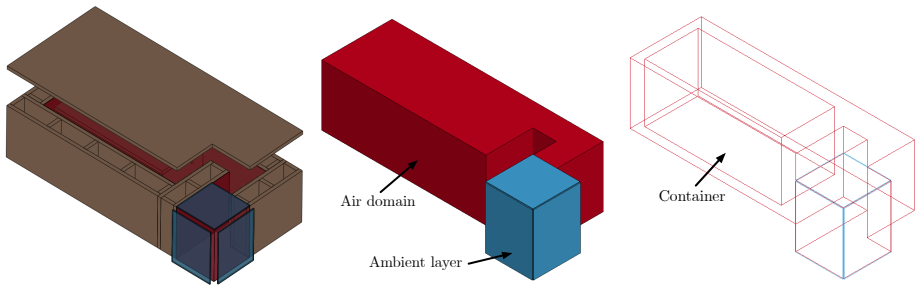

(a) (b) (c)

Fig. 5 HBC model: (a) overall view of model (3D) with air domain (shown in red); (b) air domain and ambient layer; and (c) wireframe view of the whole model showing the location of the ISO container.

The 3D numerical model was discretised with hexahedral elements with ALE formulation. This element formulation has a single integration point, commonly referred to as reduced integration. It is well known, however, that while such an approach is highly efficient from a computational point of view, under-integrated formulations can lead to the development of spurious zero energy (hourglass) modes [26]. If left uncontrolled, hourglassing can propagate throughout the model until it becomes unstable, often leading to serious convergence issues and erroneous solutions. Algorithms to control these zero energy modes should then be used to eliminate hourglassing. Through a variety of different techniques, these algorithms attempt to suppress the development and spread of hourglass deformation patterns in the model. In some applications, however, the default hourglass control set-up in LS-DYNA might lead to significant energy losses [27]. The viscous form hourglass control was used in this study [28,29].

3.2 Material modelling

Since the coupled LBE/MM-ALE method allows to only model the air domain, the numerical model can be described through the combination of a constitutive equation and an equation of state (EoS). The air is considered to be an ideal gas and the material type `*MAT_NULL` is used to define the evolution of the density of the fluid. The pressure in the air is defined by a linear-polynomial equation of state (using the keyword `*EOS_LINEAR_POLYNOMIAL`), which is linear in internal energy [30] and cubic in density. The pressure is given by

$$P = C_0 + C_1\mu + C_2\mu^2 + C_3\mu^3 + \left(C_4 + C_5\mu + C_6\mu^2\right)E \tag{2}$$

where C_i with $i = 0,\ldots,6$ are material constants, E is the specific internal energy and

$$\mu = \frac{\rho}{\rho_0} - 1 \tag{3}$$

where ρ/ρ_0 is the ratio of the current density to the reference density. The linear-polynomial EoS is used to model gases, such as air, that follow a gamma law type of equation of state. This is achieved by setting $C_0 = C_1 = C_2 = C_3 = C_6 = 0$ and $C_4 = C_5 = \gamma - 1$, where $\gamma = c_p/c_v$ is the ratio of specific heats. For an ideal gas, pressure then becomes

$$P = (\gamma - 1)\,\frac{\rho}{\rho_0}E \tag{4}$$

At time $t = 0$ equation 4 gives an initial pressure $p_0 = 100$ kPa for $\gamma = 1.4$. All relevant material properties are listed in Table 1.

Table 1 Material and equation of state properties and constants for air [20].

Material	Parameter	Value
Air	Density, ρ	1.225 kg/m^3
	$C_0 = C_1 = C_2 = C_3 = C_6$	0
	$C_4 = C_5$	0.4
	Specific internal energy, E	2.5×10^{-4} kJ/kg

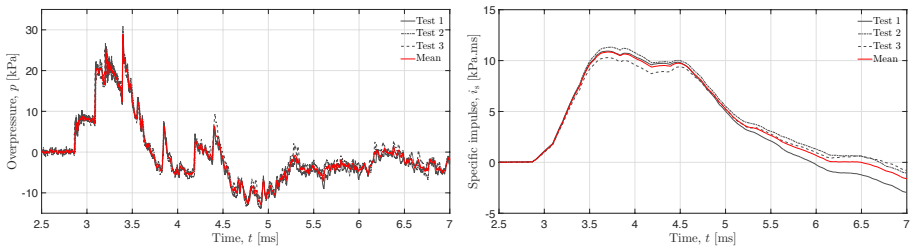

(a) (b)

Fig. 6 (a) Experimentally measured overpressures and (b) calculated specific impulse-time histories for sensor E (location shown in Figure 4), illustrating the repeatability of the experimental tests.

4 Results and discussion

The main aim of the work here presented is to investigate the complexity of the propagation of blast waves in a Hesco-Bastion survival shelter. This was achieved by combining an experimental campaign with the development of a representative numerical model, the details of which were described in the previous sections.

The consistency of the experimental tests was ensured by doing three repetitions for each stand-off distance. Figures 6(a) and (b) show the overpressure and specific impulse-time histories, respectively, obtained at sensor E, which is located on the front face of the container as shown in Figure 4(a). The specific impulse at any time t is calculated based on the overpressure-time history as the integral of the pressure from the time of arrival of the shock wave, t_a, to current time t, that is

$$i_s(t) = \int_{t_a}^{t} p(t)\mathrm{d}t \tag{5}$$

Both the negative and positive phases of the pressure-time waveform contribute to the impulse. Figure 7 shows the evolution of impulse and pressure for a typical free-air detonation. The magnitude and distribution of blast loads on a structure vary greatly with factors such as the properties of the high-explosive, the location of the detonation relative to the structure and the reinforcement of the pressure pulse through interactions with the ground or surrounding structures (e.g., reflections) [31]. These factors can lead to complex pressure profiles, as shown in the results presented here, which are associated to a confined environment where multiple reflections take place, and ultimately lead to increased pressure peaks originated from constructive interference of waves. Discrepancies between different experiments are not significant, as can be seen from the initial results shown: maximum 7% variation for the maximum overpressure and 5% for the specific impulse of first positive peak.

4.1 Ambient layer and advection method

A detailed analysis was done to study the influence of numerical model parameters such as the number of ambient layers (AL), the type of advection method (METH), mesh quality, and the time-step size. These are described and discussed in detail in the following paragraphs.

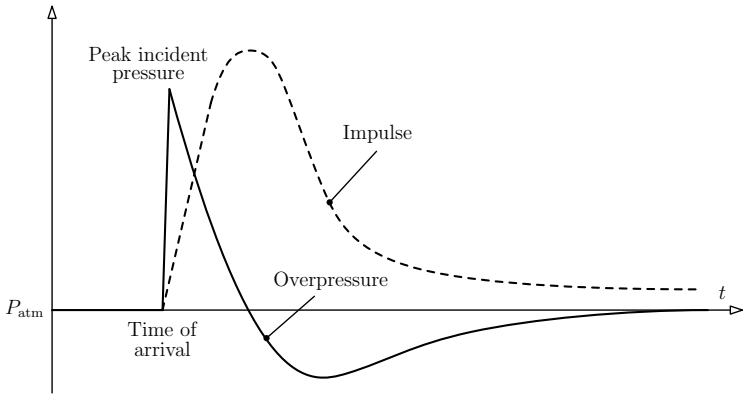

Fig. 7 Schematic representation of typical pressure and impulse waveforms (adapted from [31]).

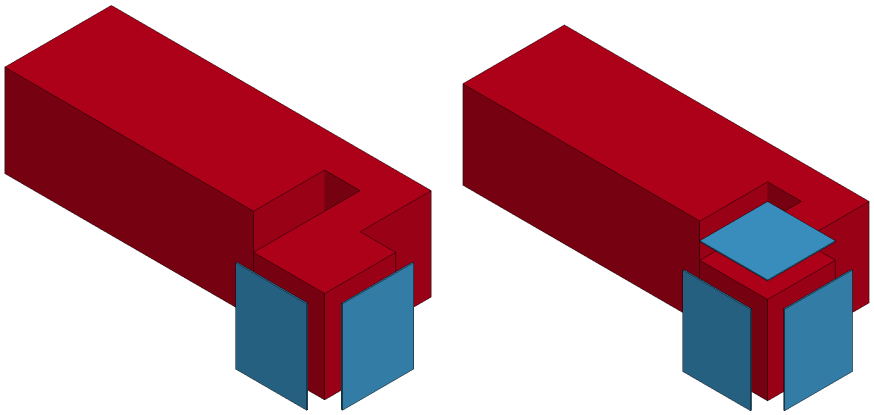

Fig. 8 Numerical model domain with exploded views of (a) two and (b) three ambient layers (shown in blue).

Han *et al.* [27] and by Lecompte *et al.* [1] have used numerical models of blast propagation in free-air using a single ambient layer for orthogonal detonations and two ambient layers for explosions on a diagonal direction, respectively. The implementation of a third ambient layer on a horizontal surface above the entrance of the shelter, as shown in Figure 8(b), was analysed numerically to assess the role of that surface on the characteristics of the shock propagation. The results in Figure 9(a) and (b) show the overpressure and specific impulse-time histories for both models — with two and with three ambient layers — compared with the experimental observations. It can be seen clearly that the implementation of a third ambient layer significantly improves the quality of the results across the whole duration of the tests. To accurately model the problem, it is thus necessary to use the third ambient layer above the entrance of the HBC, since this avoids (numerical) leakage of pressure through this surface. Consequently, all further analyses are done with three ambient layers.

The principle of the ALE formulation is based on the independence of material motion and the deformation of the finite element mesh. The freedom of deformation of the

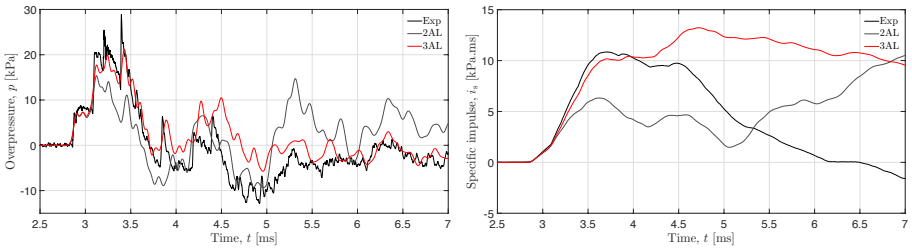

(a) (b)

Fig. 9 Comparison between experimental and numerical (a) overpressure and (b) specific impulse results using two and three ambient layers (at sensor E).

mesh offered by the ALE formulation derives from a combination of advantages from both the Lagrangian and the Eulerian approaches. A widely implemented approach to solve the ALE formulation is often referred to in mathematical literature as an operator split, where a Lagrangian followed by an Eulerian phase are performed [32]. This two-part operation is known as the advection method, where the mass, momentum and internal energy conservation equations are enforced, as is the tracking of all state variables. A transport problem is solved in this advection process. The numerical approaches used to implement the advection method are described in detail by Young [33] and Benson [34], where the Donor Cell algorithm, a first order advection method, and the van Leer algorithm, a second order advection method, are used [35].

As soon as the material is advected into a new element, it spreads across the whole element. As the van Leer equation uses a parabolic fit to transfer material flux at the element face, this formulation allows for a gradual change in material flux, as opposed to the instantaneous change in the generic algorithm [36].

Schwer [37] states that when detonation products are omitted the recommended advection algorithm is a combination of the van Leer and the Half-Index-Shift (HIS) methods. Results in Figure 10(a) and 10(b) show a comparison between the two advection methods: (i) the van Leer combined with HIS, and (ii) the Donor Cell also combined with HIS. In LS-DYNA these are referred to as `METH=2` and `METH=3`, respectively. As can be seen, there is no significant difference between the overpressure and specific impulse histories obtained with both methods for the initial stages of the blast wave interaction with the structure ($t < 3.7$ ms). Globally, both are in good agreement with the experimental results. However, the use of different advection methods affects the accuracy of the overpressure peaks. It can be seen that the van Leer algorithm captures these peaks better.

4.2 Time integration and discretisation

The incremental nature of the numerical integration procedure involves two significant approximations, one being the response of the system during each time-step, which is approximated by quadrature equations, and the other the basic assumption that the stiffness and damping properties remain unchanged during the time-step. In most cases the errors introduced by these two assumptions are small if the time-step is kept small [38]. In LS-DYNA the time-step increment is automatically calculated by default. This is done based on the material properties and assuming that the time interval between two consecutive iterations is smaller than the time the wave needs to propagate through the length of each element. This

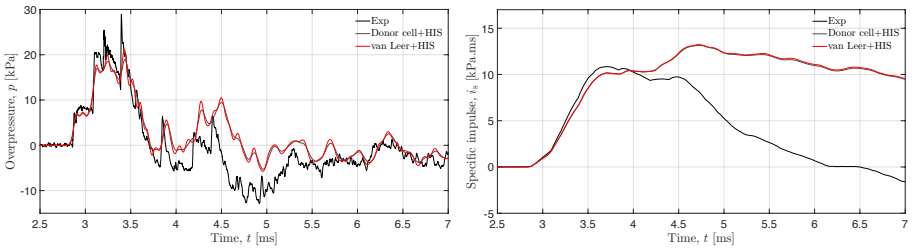

(a) (b)

Fig. 10 Experimental and numerical (a) overpressure-time history and (b) corresponding specific impulse-time history (at sensor E) for the van Leer and Half-Index-Shift (HIS) methods, and the Donor Cell combined with HIS advection methods.

is known as the Courant-Friedrichs-Lewy (CFL) condition [39]. Consequently, to ensure a stable explicit incremental integration scheme, the maximum time-step size should be

$$\Delta t \leq \frac{L_{\mathrm{e}}}{c} \tag{6}$$

The size of the time-step, Δt, is directly proportional to the characteristic length of each element, L_{e}, where c is the adiabatic speed of sound in the medium, air in this case. For hexahedral elements, this characteristic length is calculated as

$$L_{\mathrm{e}} = \frac{V}{A_{\max}} \tag{7}$$

where V is the volume of the element and $A_{\max}$ is the maximum area of the element sides [36].

The automatically calculated value of the time-step size for the numerical model presented here is $\Delta t = 5 \times 10^{-3}$ ms. This corresponds to a sound speed $c = 340$ m/s, which is the speed of sound in air at atmospheric pressure and room temperature ($T = 20^{\circ}$C), which is in agreement with the formulation presented above. Nevertheless, the shock wave travels significantly faster than the speed of sound [40], so it is important to analyse the influence of the time-step size on the convergence and numerical results. Figures 11(a) and (b) show the influence of the time step size on the obtained overpressure and specific impulse histories, compared with the experimental observations. As expected, the numerical results are in better agreement with the experimental observations with the decrease of the time-step size. This is more evident in the first positive overpressure peak (for $t < 3.6$ ms). The numerical results tend to be in worse agreement with the experimental results from the first positive overpressure onwards (see $t > 3.6$ ms in Figure 11(a) and (b)). The time-step for the analyses was chosen to be $\Delta t = 1 \times 10^{-3}$ ms.

This section also focuses on the study of mesh size effect on the quality of the numerical results. Numerical simulations were done using a range of different element sizes. The description of the meshes and the obtained results are listed in Table 2. The assessment criteria used in the present study were peak overpressure, $P_{\max}$, and specific impulse, i_{s}, to compare small-scale experimental results with the numerical results, in a similar way to Schwer et al. [41]. The specific impulse is the major parameter responsible for structural response and eventual damage under impulsive loading regimes [42], which shows the relevance of considering this parameter in the analysis.

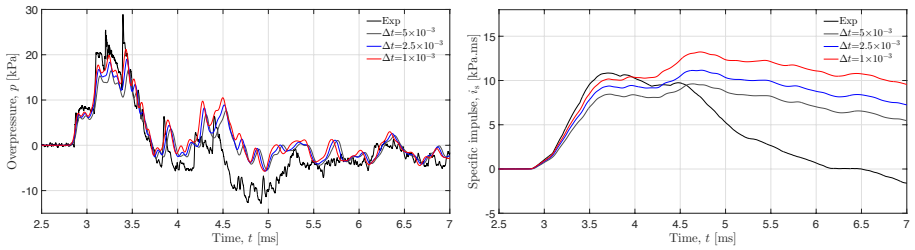

(a) (b)

Fig. 11 (a) Overpressure history and (b) specific impulse history for different integration time-step sizes (at sensor E).

Table 2 Mesh convergence details and corresponding numerical results.

Element size [mm]	Number of elements	CPU time [min]	$P_{max,exp}$ [kPa]	$P_{max,num}$ [kPa]	Error [%]	$i_{s,exp}$ [kPa.ms]	$i_{s,num}$ [kPa.ms]	Error [%]
13	24988	7	28.9	19.3	-33.2	10.8	10.9	0.9
6.5	195808	80	28.9	19.9	-31.1	10.8	10.2	-5.6
3.25	1550080	561	28.9	21.2	-26.6	10.8	10.2	-5.6

Maximum overpressure and specific impulses of first positive peak.

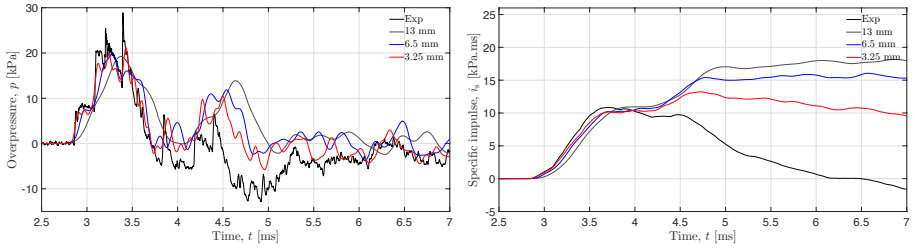

(a) (b)

Fig. 12 (a) Overpressure history and (b) specific impulse history for different element sizes (at sensor E).

Although the error for the specific impulse is 0.9% for an element size of 13 mm (see results in Table 2 and Figure 12(a) and (b)), the numerical value is calculated from a curve with inadequate qualitative agreement with the experimental results. The best match between the experimental and numerical results is obtained for an element size of 3.25 mm. Consequently, it can be concluded that the overpressure curve is strongly dependent on the element size.

Based on the analysis of both the overpressure and the corresponding specific impulse, it is noticeable that the quality of overpressure results increases with mesh refinement. For mesh sizes smaller than 3.25 mm the CPU times and memory requirements were too high. As such, the 3.25 mm mesh size was considered to be the one that leads to an optimum balance in terms of specific impulse and peak overpressure. The CPU time for this particular model was, naturally, the highest albeit still considered to be reasonable. Consequently, this was the mesh size used in the remainder of this study.

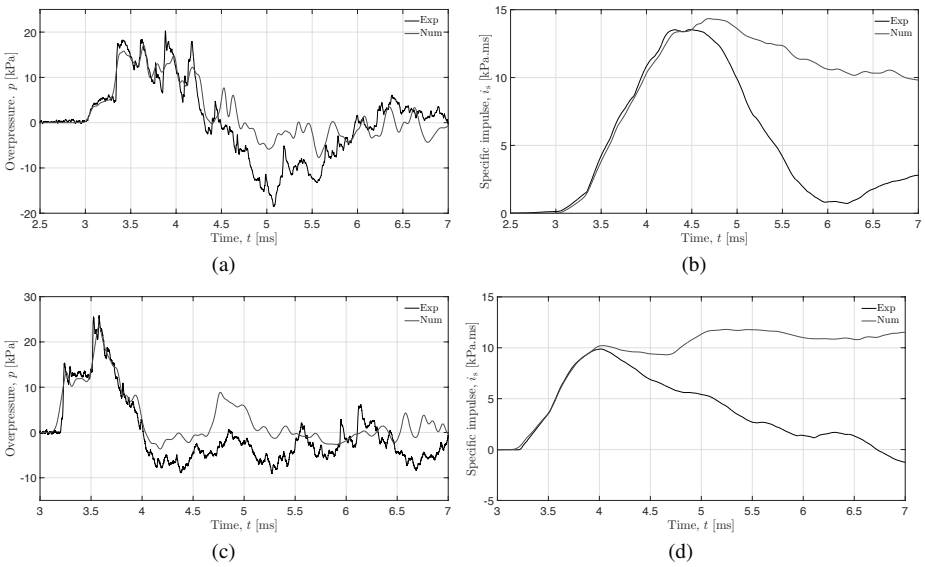

Fig. 13 Experimental and numerical overpressure and specific impulse histories (a-b) at sensor C and (c-d) at sensor A ($R = 1$ m).

4.3 Blast wave propagation

Experimental overpressure and specific impulse-time histories from the sensors at different locations were compared with the numerical results for validation, as shown in Figures 13 and 14. The major features of the recorded overpressure profiles are well captured by the numerical models, including the peak overpressure and smaller peaks resulting from the initial blast wave reflections. The differences can be quantified for the peak overpressure and the first positive specific impulse, where the absolute differences between experimental and numerical results are 2.4 and 4.4%, respectively, at sensor B for a stand-off distance $R = 1$ m.

From the results shown in Figures 13 and 14, it can also be seen that the numerical models predict well the shock front going through all the tracer points, as well as the first positive specific impulse of the blast wave. The relative errors of the computed peak overpressure and first positive specific impulse are in the range of 0 to 19% (see Table 3), confirming a good approximation of the experimental results. The exception are the measurements at sensor C for a stand-off distance $R = 0.5$ m. This discrepancy can be explained by the location of this sensor, which is not directly exposed to the blast wave, and will thus be recording a combination of incident and reflected pulses.

Regarding the entire overpressure-time curve, there is an equilibrium of positive and negative peak pressures in the experimental signal, while in the numerical curve the pressure tends to be predominantly positive. Nevertheless, the solution presented fits the experimental results well in terms of the first positive peak of the overpressure profile. This trend extents to all sensors and is clearly visible in Figures 13(b) and (d) and Figures 14(b) and (d), where the numerical specific impulse perfectly matches the experimental data up to the time corresponding to the end of the first positive overpressure peak.

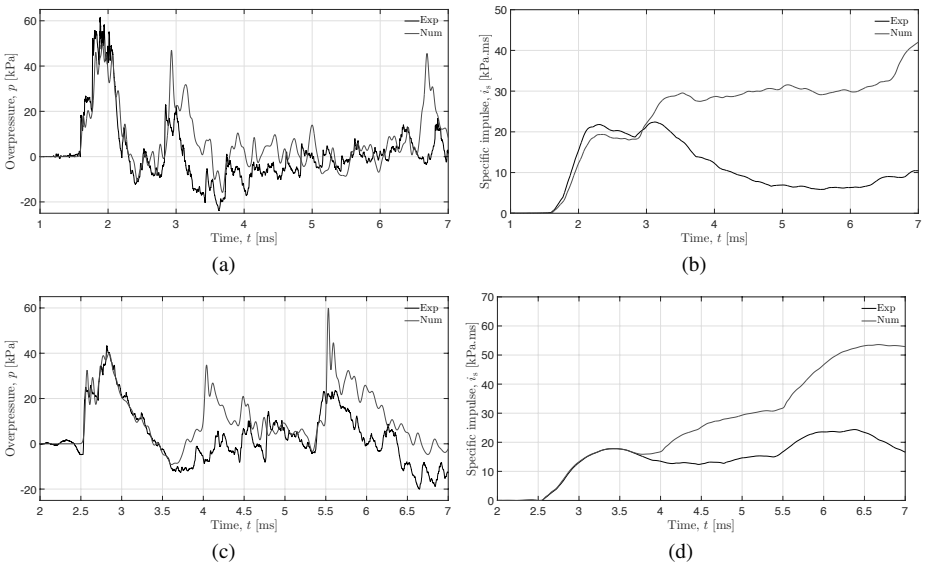

Fig. 14 Experimental and numerical overpressure and specific impulse histories (a-b) at sensor D and (c-d) at sensor B ($R = 0.5$ m).

Table 3 Overpressure, specific impulse, and relative error between computational and experimental results at different sensor locations.

R [m]	**Sensor**	$P_{\text{max,exp}}$ **[kPa]**	$P_{\text{max,num}}$ **[kPa]**	**Error [%]**	$i_{\text{s,exp}}$ **[kPa.ms]**	$i_{\text{s,num}}$ **[kPa.ms]**	**Error [%]**
1	A	25.9	23.4	-9.7	9.9	10.2	3.0
	B	20.6	21.1	2.4	9.0	9.4	4.4
	C	20.3	17.1	-15.8	13.4	13.4	0.0
	D	25.0	22.5	-10.0	9.7	10.1	4.1
0.5	A	54.7	47.0	-14.1	20.3	19.5	-3.9
	B	43.4	40.0	-7.8	18.0	17.8	-1.1
	C	44.1	32.3	-26.8	27.9	24.6	-11.8
	D	61.7	50.0	-19.0	21.0	19.4	-7.6

Maximum overpressure and specific impulses of first positive peak.

The complexity of the blast wave propagation due to the superposition of multiple reflected waves make these experiments a useful case study for validation of numerical models. The propagation of the blast waves as predicted by the numerical model is shown in Figures 15 and 16. The pressure contours and wave front propagation allow a better understanding of the interaction of the blast waves with the surrounding infrastructure. Results shown in Figures 15(a) and 16(a) show the first interaction with the surrounding environment, and further progression of the incident wave at ground level. The vertical development of the wave is also visible in Figure 16.

Approximately 1.8 ms after the detonation, the blast wave reaches the entrance corridor of the Hesco-Bastion compound (HBC). The pressure increase due to the confinement is visible from this moment onwards. Shock reflection-diffraction phenomena occur every time the shock wave encounters an obstacle, such as vertical walls [43]. These can be observed, for example, at $t = 2.3$ ms at the corners of the entrance of the compartment (both

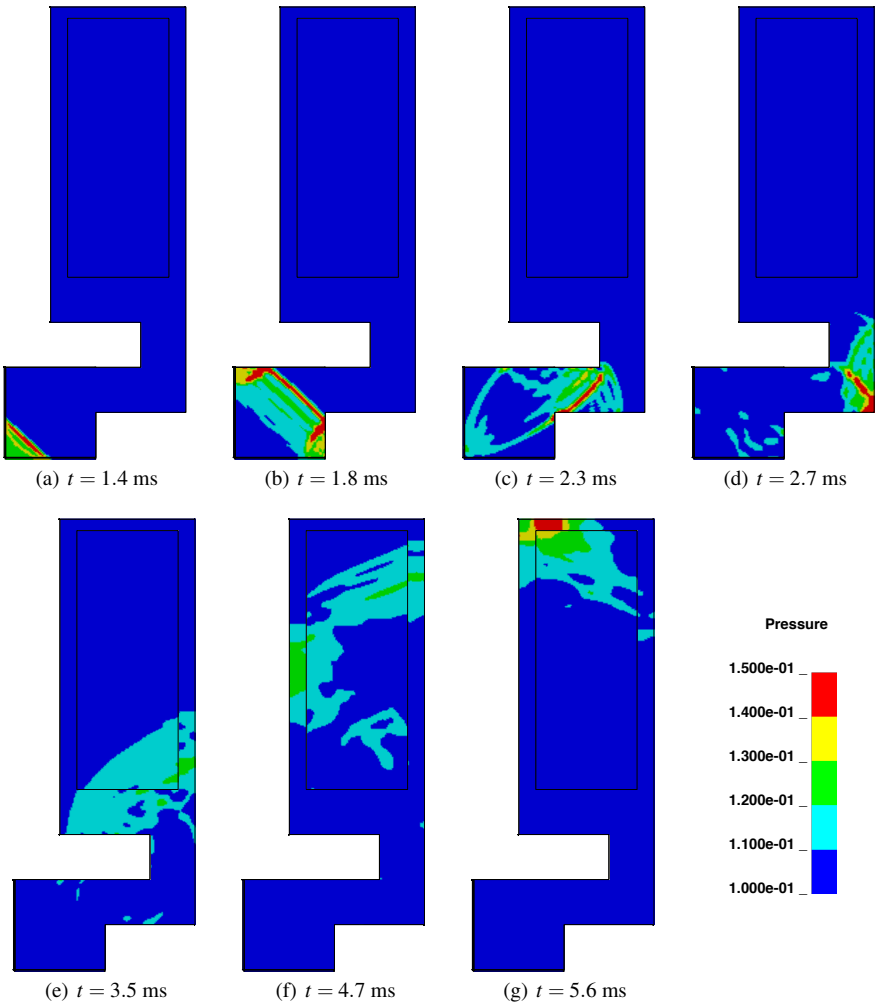

Fig. 15 Two-dimensional view of the blast wave propagation pressure profiles (in MPa) in the Hesco-Bastion container configuration model at different time steps.

convex and concave), as shown in Figures 15(c) and (d) and Figures 16(c) and (d). Pressure localisation and amplification can also be observed in Figures 15(d) and 16(d), where the blast waves have overlapped, leading to a (additive) wave superposition. Once inside the HBC, the shock wave splits along both sides and above the ISO container. The split lateral waves meet at the back face of the ISO container leading to a constructive interaction and the consequent increase in pressure, which can be seen in Figures 15(g) and 16(g). This effect is further amplified due to the converging pressure wave travelling above the ISO container, also shown in Figures 15(e–g) and 16(e–g).

The results presented here reinforce the complexity of blast wave propagation inside confined compartments such as the HBC shelter studied in this work. In terms of pressure and impulse on the outer surfaces of the ISO container and for situations such as the one described, the critical points are those located furthest away from the entrance, where the

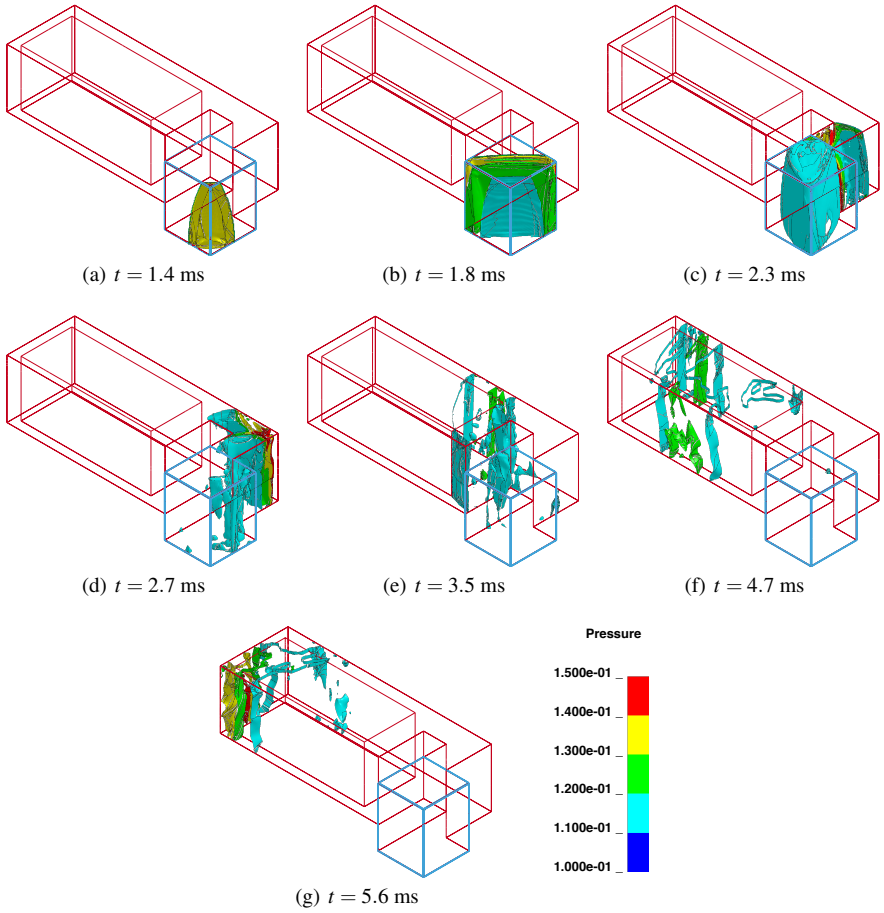

(a) $t = 1.4$ ms (b) $t = 1.8$ ms (c) $t = 2.3$ ms

(d) $t = 2.7$ ms (e) $t = 3.5$ ms (f) $t = 4.7$ ms

(g) $t = 5.6$ ms

Fig. 16 Three-dimensional blast wave propagation pressure profiles (in MPa) in the Hesco-Bastion container configuration model at different time steps.

constructive interference described above happens. In terms of HBC shelter design, one possible way to minimise this would be to add a second entrance/exit at that location, to allow for venting to occur. Design solutions like this, however, add vulnerability to the shelter system.

5 Conclusions

The blast wave propagation inside a Hesco-Bastion compound (HBC) survival shelter is assessed experimentally using a small-scale model of a real configuration subjected to the detonation of explosive charges at different locations close to the entrance of the HBC. A set of three-dimensional numerical models are proposed to study the propagation and interaction of shock waves in the HBC.

The main aims of this work are to obtain and validate predictions of overpressure and impulse-time histories, to study the details of blast wave propagation and interaction within

the confined space, applying computational fluid dynamics techniques, and to analyse the structural consequences in terms of shelter design.

The obtained results show good agreement between experimental and numerical observations for the first positive overpressure peak, when compared to successive peaks, which is also supported by the observations of Huang et al. [44] in a study concerning blast wave propagation in urban environments. Reflections due to confined geometries can be highly complex and often difficult to capture with numerical methods, unless no compromise is necessary for numerical efficiency. The proposed models may also be used, albeit only qualitatively, to analyse the effects of multiple reflections on the structural response. The analysis of such effects can be used to inform new shelter designs and changes to existing ones.

Acknowledgements The authors acknowledge the technical advice and contributions of Frederik Coghe, Bruno Reymen, Peter Michiels and Tony Tuts.

References

1. D. Lecompte, R. De Schepper, B. Belkassem, D. Kakogiannis, B. Reymen and J. Vantomme, A modular building-block system for lab-scale explosive testing of urban type configurations, 23rd Military Aspects of Blast and Shock, Oxford (2014)
2. G.F. Kinney and K.J. Graham, Explosive shocks in air. Springer, New York (1985). https://doi.org/10.1007/978-3-642-86682-1
3. W. E. Baker, P. A. Cox, P. S. Westine, J. J. Kulesz and R. A. Strehlow, Explosion hazards and evaluation. Elsevier Science B. V., Amsterdam (1983). https://doi.org/10.1016/0010-2180(85)90099-9
4. B. Julien, I. Sochet and T. Vaillant, Impact of the volume of rooms on shock wave propagation within a multi-chamber system, Shock Waves, 26, 87-108 (2016). https://doi.org/10.1007/s00193-015-0603-2
5. P. D. Smith, G. P. Whalen, L. J. Feng and T. A. Rose, Blast loading on buildings from explosions in city streets, Proceedings of the Institutions of Civil Engineers - Structures & Buildings, 46, 47-55 (2000). https://doi.org/10.1680/stbu.2001.146.1.47
6. R. C. Ripley, B. von Rosen, D. V. Ritzel and D. R. Whitehouse, Small-scale modeling of explosive blasts in urban scenarios, 21st International Symposium on Ballistics, Adelaide (2004)
7. A. M. Remmenikov and T. A. Rose, Modelling blast loads on buildings in complex city geometries, Computers and Structures, 83, 2197-2205 (2005). https://doi.org/10.1016/j.compstruc.2005.04.003
8. P. D. Smith and T. A. Rose, Blast wave propagation in city streets - an overview, Progress in Structural Engineering and Materials, 8, 16-28 (2006). https://doi.org/10.1002/pse.209
9. C. Fouchier, D. Laboureur, L. Youinou, E. Lapebie and J. M. Buchlin, Experimental investigation of blast wave propagation in an urban environment, Journal of Loss Prevention in The Process Industries, 49, 248-265 (2017). https://doi.org/10.1016/j.jlp.2017.06.021
10. B. W. Skews and W. R. Law, The propagation of shock waves in a complex tunnel system, Journal of The South African Institute of Mining and Metallurgy, 91, 137-144 (1991)
11. P. D. Smith, G. C. Mays, T. A. Rose, K. G. Teo and B. J. Roberts, Small scale models of complex geometry for blast overpressure assessment, International Journal Impact Engineering, 12, 345-360 (1992). https://doi.org/10.1016/0734-743X(92)90112-7
12. F. Rigas and S. Sklavounos, Experimentally validated 3-D simulation of shock waves generated by dense explosives in confined complex geometries, Journal of Hazardous Materials, 121, 23-30 (2005). https://doi.org/10.1016/j.jhazmat.2005.01.031
13. P. E. Sauvan, I. Sochet and S. Trélat, Analysis of reflected blast wave pressure profiles in a confined room, Shock Waves, 22, 253-264 (2012). https://doi.org/10.1007/s00193-012-0363-1
14. C. Geretto, S. C. Yuen and G. N. Nurick, An experimental study of the effects of degrees of confinement on the response of square mild steel plates subjected to blast loading, International Journal Impact Engineering, 79, 32-44 (2015). https://doi.org/10.1016/j.ijimpeng.2014.08.002
15. T. Anthistle, D. I. Fletcher and A. Tyas, Characterisation of blast loading in complex, confined geometries using quarter symmetry experimental methods, Shock Waves, 26, 749-757 (2016). https://doi.org/10.1007/s00193-016-0621-8
16. F.C. Salvado, A.J. Tavares, F. Teixeira-Dias, J.B. Cardoso, Confined explosions: The effect of compartment geometry, Journal of Loss Prevention in the Process Industries, 48, 126-144 (2017). https://doi.org/10.1016/j.jlp.2017.04.013

17. B. Luccioni, D. Ambrosini and R. Danesi, Blast load assessment using hydrocodes, Engineering structures, 28, 1736-1744 (2006). https://doi.org/10.1016/j.engstruct.2006.02.016
18. A. Zyskowski, I. Sochet, G. Mavrot, P. Bailly and J. Renard, Study of the explosion process in a small scale experiment - structural loading, Journal of Loss Prevention in the Process Industries, 17, 291-299 (2004). https://doi.org/10.1016/j.jlp.2004.05.003
19. P. D. Smith and J. G. Hetherington, Blast and ballistic loading of structures. Butterworth-Heinemann, Oxford (1994)
20. H. Ousji, B. Belkassem, M. A. Louar, D. Kakogiannis, B. Reymen, L. Pyl and J. Vantomme, Parametric study of an explosive-driven shock tube as blast loading tool, Experimental Techniques, 40, 1307-1325 (2015). https://doi.org/10.1111/ext.12179
21. C. N. Kingery and G. Bulmash, Air-Blast parameters from TNT spherical air burst and hemispherical surface burst, Technical report ARBRL (TR-02555), Ballistic Research Laboratory, Maryland (1984)
22. U.S. Department of the Army, Fundamentals of protective design for conventional weapons, Technical manual (TM5-855-1), U.S. Army Engineer Waterways Experiment Station, Washington DC (1986)
23. T. P. Slavik, A coupling of empirical explosive blast loads to ALE air domains in LS-DYNA, 7^{th} European LS-DYNA Conference, Austria (2009). https://doi.org/10.1088/1757-899X/10/1/012146
24. M. Shuaib and O. M. A. Daoud, Numerical analysis of RC slab under blast loads using the coupling of LBE and ALE method in LS-DYNA, fib Symposium, Cape Town (2016)
25. Livermore Software Technology Corporation, LS-DYNA User Manual: Volume I (Version R7.1), Livermore, California (2014)
26. G. R. Consolazio, J. H. Chung and K. R. Gurley, Impact simulation and full scale crash testing of a low profile concrete work zone barrier, Computers and Structures, 81, 1359-1374 (2003). https://doi.org/10.1016/S0045-7949(03)00058-0
27. Y. Han and H. Liu, Finite element simulation of medium-range blast loading using LS-DYNA, Shock and Vibration, 2015, 1-9 (2015). http://dx.doi.org/10.1155/2015/631493
28. A. Alia and M. Souli, High explosive simulation using multi-material formulations, Applied Thermal Engineering, 26, 1032-1042 (2006). https://doi.org/10.1016/j.applthermaleng.2005.10.018
29. D. P. Flanagan and T. Belytschko, A uniform strain hexahedron and quadrilateral and orthogonal hourglass control, International Journal for Numerical Methods in Engineering, 17, 679-706 (1981). https://doi.org/10.1002/nme.1620170504
30. Livermore Software Technology Corporation, LS-DYNA User Manual: Volume II Material Models (Version R7.1), Livermore, California (2014)
31. Federal Emergency Management Agency, Reference manual to mitigate potential terrorist attacks against buildings, FEMA 426, Department of Homeland Security, U.S. (2003)
32. K. Mahmadi, N. Aquelet and M. Souli, New mesh relaxation technique in Multi-Material ALE applications, Emerging Technology in Fluids, Structures and Fluid-Structure Interactions, 1, 135-140 (2004). https://doi.org/10.1115/PVP2004-2863
33. D. L. Youngs, Time-dependent multi-material flow with large fluid distortion, Numerical Methods for Fluids Dynamics, 24, 273-285 (1982)
34. D. J. Benson, Momentum advection on a staggered mesh, Journal of Computational Physics, 100, 143-162 (1992). https://doi.org/10.1016/0021-9991(92)90316-Q
35. B. Van Leer, Towards the ultimate conservative difference scheme. IV. A new approach to numerical convection, Journal of Computational Physics, 23, 276-299 (1977). https://doi.org/10.1016/0021-9991(77)90095-X
36. Livermore Software Technology Corporation, LS-DYNA Theory Manual, Livermore, California (2006)
37. L. Schwer, A brief introduction to coupling load blast enhanced with Multi-Material ALE: the best of both worlds for air blast simulation, 9^{th} LS-DYNA Forum, Bamberg (2010)
38. S. Y. Chang and C. L. Huang, A new family of explicit time integration methods, IOP Conference Series: Materials Science and Engineering, 10 (2010). https://doi.org/10.1088/1757-899X/10/1/012145
39. R. Courant, K. Friedrichs and H. Lewy, On the partial difference equations of mathematical physics, IBM Journal of Research and Development, 11, 215-234 (1967). https://doi.org/10.1147/rd.112.0215
40. W. Weibull, Explosion of spherical charges in air: travel time, velocity of front, and duration of shock waves, Technical report, Ballistic Research Laboratories, Maryland (1950)
41. L. E. Schwer, M. D. Netherton and M. G. Stewart, Comparisons of University of Newcastle free air blast data with Conwep and LS-DYNA simulations, 23^{rd} Military Aspects of Blast and Shock, Oxford (2014)
42. P. S. Westine and W. E. Baker, Energy solutions for predicting deformations in blast-loaded structures, Technical report, Southwest Research Institute, Texas (1975)
43. G. Chen and M. Feldman, Shock reflection-diffraction phenomena and multidimensional conservation laws, Proceedings of Symposia in Applied Mathematics (2009)
44. Y. Huang, M. R. Willford and L. E. Schwer, Validation of LS-DYNA MMALE with blast experiments, 12^{th} International LS-DYNA Users Conference, Detroit (2012)